Chapter 13
Composite Plate Response to Shock Wave Loading

Douglas Jahnke, Vahid Azadeh Ranjbar, and Yiannis Andreopoulos

Abstract The mechanical response and characterization of composite materials under transient dynamic loading caused by shock or blast wave impingement is not well understood. Air blast is associated with a fast-traveling, high-pressure shock front followed by a lower pressure expansion wave. The timescales associated with the shock front are typically 10^3 faster than those associated with the expansion waves which follow. A new split-view Time-Resolved Stereo Digital Image Correlation system has been developed capable of measuring time dependent information of three component displacement vectors on two dimensional surfaces in a shock tube facility where transient aerodynamic loads on material specimens develop over the short time associated with the shock wave reflection time scales. To validate the techniques we embedded strain gauges in a S-2 glass epoxy 12.7 mm thick composite test specimen during in-house using vacuum assisted resin transfer molding fabrication. High-frequency-response, semiconductor, strain gauges were used in various combinations and locations in order to measure the transient strain rate during the impingement of the shock wave. In addition to strain gauges PZT transducers were also embedded which helped measure the frequency response of the test plate. In-house fabricated composite plates were tested under three different boundary conditions: clamped, quasi-simply supported, and bolted. Different displacements and deformation patterns were observed in each of these cases.

Keywords Composites • Shock wave • Boundary conditions

13.1 Introduction

Composites, heterogeneous material systems, are believed to exploit synergistic effects from the combination of dissimilar materials thereby developing unique property combinations not possible using other means. One class of composites is high-performance fiber-reinforced polymer (FRP). These have been increasingly used in structural applications over the last 30 years. Relative to traditional materials they have high specific-stiffness, high specific-strength, low specific-weight and are able to absorb significant energy from impacts. There are a many types of fibers and matrices available to use in FRPs. Each fiber and matrix combination can have different properties. Besides the variations in material properties in the fibers or matrices, the strength of the interface bond between the fiber and the matrix, and between the laminae as well as the lay-up sequences, ply orientations, and different forms of fiber arrangements within the matrix (particulate, planar, 2D/3D woven) all influence the final properties of the composite system. This allows composite properties such as modulus of elasticity, density, wave propagation speeds, and thermal conductivity to be adjusted. All these features have made FRP composites attractive as replacements for traditional materials.

These features also make them difficult to characterize in a systematic way. This vast number of variables makes it challenging to predict the overall structural and acoustic properties of a FRP composite from the details of the materials and construction. Thus, knowledge of the response of composite materials under dynamic loading is essential to develop a better understanding of its performance as a structural material. While such information starts to be slowly available very little is known about the behavior of such materials under the effects of dynamic mechanical extremes. Understanding such material systems requires performance testing data of the effects of dynamic events in order to fully document the behavior of this material.

D. Jahnke • V.A. Ranjbar • Y. Andreopoulos (✉)
Department of Mechanical Engineering, The City College of New York, 160 Convent Avenue, New York, NY 10031, USA
e-mail: andre@ccny.cuny.edu

D. Casem et al. (eds.), *Dynamic Behavior of Materials, Volume 1*, Conference Proceedings
of the Society for Experimental Mechanics Series, DOI 10.1007/978-3-319-41132-3_13

13.2 Thin Composite Plate Response to Pressure Loading

The mechanical response and characterization of composite materials under transient dynamic loading caused by shock or blast wave impingement is not well understood. Air blast is associated with a fast-traveling, high-pressure shock front followed by a lower pressure expansion wave. The timescales associated with the shock front are typically 10^3 faster than those associated with the expansion waves [1]. Impingement of blast waves on structures result in a reflection of the wave off the surface followed by a substantial transient aerodynamic load which can cause significant deformation and damage to the structure. In addition, a complex aeroelastic interaction between the blast wave and the structure develops that can induce reverberation within an enclosure and cause substantial overpressure through multiple reflections of the wave. This reverberation can cause permanent hearing loss and both physiological and psychological damage. The response of advanced composite materials to dynamic loading caused by fast moving shock waves is associated with such thermomechanical extremes. This is relevant to a broad range of applications environments such as multifunctional survivability requirements of civilian or military vehicles. In addition, establishing their structural integrity under dynamic conditions at high strain rates and their post-impact behavior become pre-requisite in such crucial applications.

The assessment of the effects of blasts on structural systems was studied systematically after World War I. An early published work was Hopkinson's study of pressure from high explosives or bullet impacts [2]. One of the earliest analyses related to structures subjected to air-blast loading in the literature was performed by Taylor [3], where he developed a solution for a one-dimensional wave impinging on a free-standing plate to compute the momentum transmitted to the plate by the shock pulse. The prediction and measurement of the structural response of ship panels to free-field air-blast explosions were first investigated by Houlston et al. [4]. In this research square plates and stiffened panels subjected to air-blast and underwater shock loads were investigated. Later, assuming a form of displacement function and a modified Friedlander equation reflected blast overpressure loading that exponentially decays with time.

Gupta et al. [5] conducted a single-degree-of-freedom elastodynamic analysis of the response of a rectangular plate subjected to an explosive blast. Beshara [6] investigated the prediction of dynamic effects of unconfined explosions needed for the structural analysis of blast-loaded above-ground structures. Türkmen and Mecitoğlu [7, 8] carried out a study on the dynamic behavior of laminated composite plates subjected to blast loading. In this study, theoretical analysis and experiment results of the strain time histories were obtained.

Recently Xue and Hutchinson [9] studied the quasi-static dynamic responses of clamped circular sandwich plates subject to uniformly distributed impulsive loads. Numerical analysis on the plate neglecting the effects of fluid-structure interaction was carried out and a new constitutive relation for sandwich plates was introduced as well [10]. In similar research, the dynamic response of a clamped sandwich beam/plate was assessed. The fluid-structure interaction effect was evaluated utilizing Taylor's approximation by including a segregated fluid-structure interaction phase in research by Deshpande, Fleck, and Qui [11, 12]. Tekalur et al. [13] experimentally studied the effect of blast loading on both an E-glass fiber composite and carbon fiber composite material, by simulating a blast in a shock tube. Results suggested that the E-glass fiber composite experienced progressive damage during high-rate loading, whereas the carbon fiber composite experienced sudden failure. Similar work was conducted by Pankow, et al. [14].

The recent work by Gong and Andreopoulos [15] investigating the impact of shock waves on monolithic (aluminum and steel) and composite material plates has shown that, the interaction between the blast and the structure is mutual. Due to the elastic deformation of the plates and their reverberation, strong acoustic waves were generated on the external side of the impact which carry a significant signature of the plates' properties. Composite plates were found to suppress several of the modes of the wave patterns while metallic ones demonstrate a rich variety of interacting modes. The amplitude of the excited acoustic waves, however, was higher in the case of composite plates than in the case of steel plates. The frequency content of the strain signals on the surface of composite plates was not always the same with the content of the surface acceleration measured in free vibration experiments. Calculations using a coupled system of equations between the fluid and solid phases of monolithic materials provided predictions in good agreement with the measured values of modal frequencies. These theoretical results were also in agreement with the classical modal analysis results by using the Poisson-Kirchhoff theory for thin plates under axisymmetric or non-axisymmetric conditions. In addition to their analytical and theoretical work, the experimental results were predicted by a fully coupled computational model developed by Gong and Andreopoulos [16, 17] in which an unstructured adaptive mesh flow solver of second order accuracy in finite volume formulation, a finite element structure solver and a moving mesh algorithm were implemented in the numerical simulation of the interaction between a shock wave and a structure. This fully coupled approach accounted for the effects associated with the mutual interaction for the first time. The results illuminated complicated flow phenomena and structure vibration patterns, which in order to be detected experimentally require capabilities beyond those available by current experimental techniques. The numerical simulations also successfully modeled the aero-acoustic damping effects on the structure, which do not exist in previous numerical models. Further analysis of the results showed that the mutual interaction is not linear and that the non-linearity

arises because the wave propagation in the fluid is not linear and it cascades a non-linear and non-uniform loading on the plate. Non-linearity intensifies when the plate is vibrating at high frequency while the wave propagation speed is low.

A blast produces transient loading of very short duration on a structural element. This loading is associated with the timescale of the shock reflection over the surface of the structure is (on the order of 1 μs). Because of the highly transient nature of the loading, the response of the structural element evolves over different timescales. It is well known that the material response in part determines the structural response. High shearing rates occur during the impact of the shock wave front on the structural element because of the extremely short timescales of the flow. Relaxation of these high shearing rates takes place immediately after the shock wave impact during the passage of the expansion wave which is associated with timescales that are 10^3 times or more slower than those of the shock wave.

In the timescale on the order of duration of the shock wave reflection, the transient response is localized and is governed by the wave propagation in the material. This response evokes a material response at the speed of stress development due to wave propagation in the material. Therefore, the structural response at the very short timescales produces strain rates higher than 10 s^{-1}. This initial response is significant as glass-polymer composites have shown strain rate effects resulting in strength increases of up to 20 % in this range in work by Khan et al. [18]. With time, the response of the structure evolves to produce vibration of the entire structural element at frequencies which are determined by the stiffness of the element and the boundary conditions. The vibrational response of the structural elements usually occurs on the millisecond timescale and produces strain rates in the range of 0.1–1.0 s^{-1}. Full-scale experiments involving actual geometries and charges are quite involved and costly, both in terms of preparation and measurements.

Moreover, full-scale testing of realistic blast scenarios is often prohibitively expensive and time consuming. Even the smallest of these full-scale tests can require explosive charges in the medium to extreme categories and outdoor laboratory experimentation [19]. At this scale, instrumentation becomes difficult and expensive, often yielding only point-wise piezoelectric pressure profiles at limited locations and a qualitative rather than quantitative evaluation of material deformation [20]. For these reasons, scaled-down experiments are highly desirable. However, the validity of such experiments has to be proven since scaling is not straightforward in all blast events.

The major advantage of a laboratory simulation as opposed to field measurements is its controllable environment which can provide a platform for systematic investigation of complex phenomena with well-established initial and boundary conditions. This is critically important in basic research where a better understanding of the underlying physics is sought or high fidelity experimental data are needed to test and verify advanced computational methods with specific predictive capabilities. In the case of monolithic materials, Justusson, et al. used a laboratory shock tube to examine aluminum deformation at high rates [21]. In the particular case of testing composite materials under blast loading existing methodologies are several and diverse since there is not an accepted standard. A tensile test, for instance, is a classic example of a widely used testing methodology (for example see ASTM D638-10) to establish the bulk properties of materials. An additional advantage to laboratory testing is the ability to vary boundary conditions.

Tekalur et al. [13] used a simply supported bending configuration to study the mechanical behavior and damage of composite specimens by static and blast loading . A shock tube apparatus was utilized to generate a planar shockwave with a controlled overpressure level. A flat rectangular panel was held in front of the end of the muzzle section. Thus the blast wave load is initially supplied over a circular area of the rectangular specimen which is simply supported. However, as the specimen is deformed the contact surface between the specimen and the shock tube wall decreases and gas pressure is applied beyond the original opening of the tube. Strain gauges are often used to measure strain rates as a function of time at specified locations on the surface of the material [15]. While a clamped boundary condition is a basic calculation analytically, it can be hard to achieve in the lab. Nurick et al. explored the effect of a clamped boundary condition on the onset of necking and tearing for circular plates [22]. Variation of the edge of the clamped boundary between a sharp edge and radii of 1.5 and 3.2 mm led to changes in deflection and the onset of thinning and tearing.

Most laboratory-scale research focuses on the deformation of plates subjected to blast loads. Nurick et al. [23] performed most of the initial work and established standard terms for the qualitative classification of steel plate failure modes and plate deformation measurement [22]. These tests include post-test measurements of maximum plate deflection and qualitative plate shape [23]. According to [23–25] the modes of failure are classified as:

- *Mode I:* Large plastic deformation without tearing of the specimen
- *Mode II:* Tensile tearing partial or complete at supports
- *Mode III:* Plastic shear sliding at supports.

Approaches using a shock tube platform appear to have certain distinct advantages over approaches using detonations. A major one is that the shock front in the shock tube is planar, thus yielding uniform pressure behind it which loads the structure. This simplifies the geometry and boundary conditions and therefore allows for a better evaluation of modeling issues associated with numerical simulations of the phenomena involved. In contrast, shock wave fronts generated by

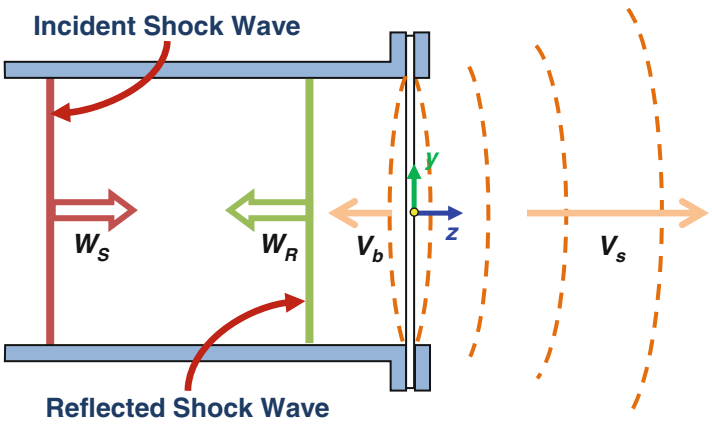

Fig. 13.1 Sound wave excitation through shock impingement

detonations are three dimensional in space and lead to complex pressure loadings which can mask the underlying basic physics of the impact. Once the physics of the impact is better understood in simple geometries then the next level of complication can be introduced.

The complicated interactions under investigation need to be set up by using a simple, yet relevant geometry of the composite material structure and simplified flow fields which have the potential to reveal basic features of the associated phenomena.

The pressure behind the incident shock wave, p_2, remains constant across the flow field before the shock reflection. As the shock wave contacts the surface of the end wall where the composite plate is installed, the process of reflection starts, the plate is loaded and deformation begins. If the plate were a rigid body the pressure behind the reflected shock, p_5 and would be given by the relation:

$$\frac{p_5}{p_2} = \frac{\left[\frac{\gamma+1}{\gamma-1} + 2\right]\frac{p_2}{p_1} - 1}{\frac{p_5}{p_2} + \left[\frac{\gamma+1}{\gamma-1}\right]}$$

When the plate is elastic, its deformation starts with the initial contact between the shock wave and the surface; however, it is not instantaneous. In tests with carbon and glass fiber composites, Arora et al. saw initial displacements lag between 1 and 2 ms behind shock wave impingement [26]. According to [27] during the initial displacement of the accelerating plate towards the $z > 0$ direction, expansion waves will be shed off in the $z < 0$ direction, the direction of the reflected shock, and compression waves will be shed off in the $z > 0$ direction on the external side of the plate. During the decelerating displacement of the plate in the other direction compression waves will be shed in the $z < 0$ direction behind the reflected shock wave and acoustic waves in the exterior side of the plate (see Fig. 13.1).

Another characteristic shared by composites is the ability to attenuate shock through resonance behavior. Work by Oved et al. showed resonance behavior due to wave reflections in the layers of the composite [28]. In particular this behavior, unexpectedly proved to be important at higher stresses (outside the linear elastic region) where elasto-plastic behavior was observed.

The fracture, damping, and stiffness properties of a composite also affect its ability to absorb energy and are dependent on the make-up and geometry of individual composite materials. In one case, Gibson et al. showed that adding a polymeric interleave in composite laminates can improve both damping and fracture toughness [29]. Other researchers such as Koratkar et al. [30], Zhou et al. [31], and Rajoria and Jalili [32] have shown that tremendous increases in the loss modulus of polycarbonates and epoxies have resulted from the addition of nanoparticles such as carbon nanotubes.

Previous work by Gupta and Nagesh [25] has shown that there is some sensitivity in the results, particularly on the onset of thinning and tearing at the boundary, to boundary fixation conditions.

13.3 Experimental Facilities

The experiments were carried out in the large-scale Shock Tube Research Facility of the Department of Mechanical Engineering at CCNY. The facility is partially shown schematically in Fig. 13.2 and is described in detail by Briassulis et al. [33] It has been used extensively for research on shock wave interactions with turbulence and vortices [1, 34, 35]. In the

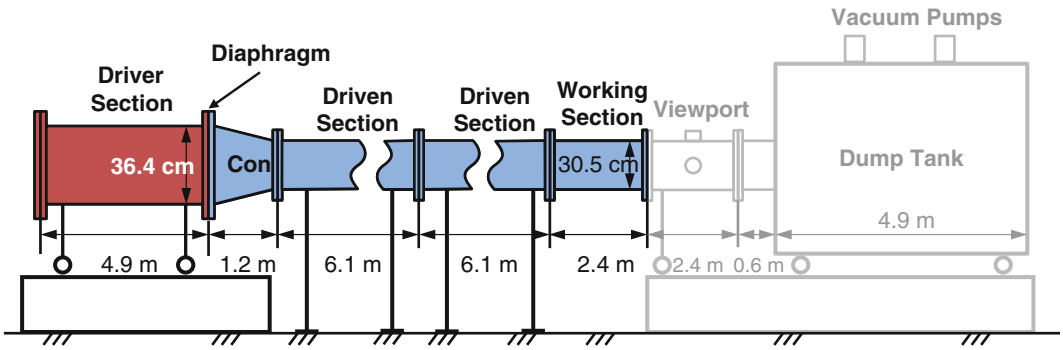

Fig. 13.2 Schematic of the CCNY high-resolution shock tube facility, with the unused features shown in gray

preset case it was used to study the impingement of shock waves on thin composite plates. The specimen was mounted at the end flange of the working section.

The rupture of the diaphragm between driver and driven sections released a shock wave which traveled downstream at pressure p_2 to the end of the working section where the test plates were mounted. The shock tube as configured for these experiments was 18.5 m (61′) in length with a working section 30.5 cm (12″) in diameter. The pressure in the shock tube was measured by transducers in the working section.

Aluminum diaphragms were used for all early experiments. These plates were 380 mm (15″) in diameter and 3.2 mm (1/8″) thick. A cross was machined to a specific depth to control the pressure at rapture (p_4). At lower pressures, up to around 690 kPa (100 psig), the aluminum diaphragms performed well. At higher pressures, the depth of the machined cut led to unreliable performance. Another material frequently used for diaphragms in shock tubes is polyethylene terephthalate (PET) commonly known by the DuPont trademark name Mylar. Later experiments were performed using 0.254 mm (10 mil) PET as the diaphragm material. A single layer of PET ruptured around 275 kPa (40 psig). Multiple layers have been used to reach higher pressures although the relationship between layers and pressure was found to be nonlinear and not entirely predictable.

13.4 Boundary Conditions

As mentioned earlier the work there is some sensitivity of the results to boundary fixation conditions [25]. Our initial results also provided indications that this is the case. In our work we configured three different boundary conditions, the original boundary condition which is referred to as clamped and two additional, quasi-simply supported and bolted. Descriptions and illustrations of the three boundary conditions are provided below.

13.4.1 Clamped

The clamped boundary condition was the as-built configuration of the shock tube for holding a circular test specimen. Figure 13.3 shows an illustration with an exploded view. The test specimen and gasket are held to the end of working section by the retaining ring. The end of the working section has a boss around the shock tube opening that fits into a rabbet in the retaining ring creating a tight seal. In order to minimize sensitivity of the particular boundary conditions on the vibrational and deformational pattern of the plate and to avoid introducing artificial nodes, additional care was taken in the way the bolts were tightened. The bolts are tightened in stages following a standard star-pattern as often specified for large pipe installations. First, the bolts are tightened snugly, in a star pattern, using an air powered impact wrench. It is important at this stage not to over tighten bolts thereby preventing the retaining ring from seating properly. Next, a torque wrench is used to tighten the bolts to the specified torque, again using a star pattern. Two passes were made using the torque wrench to ensure proper seating. If excessive movement was observed in the bolts on the second pass, i.e., a turn greater than a few degrees was required, a third pass would be made.

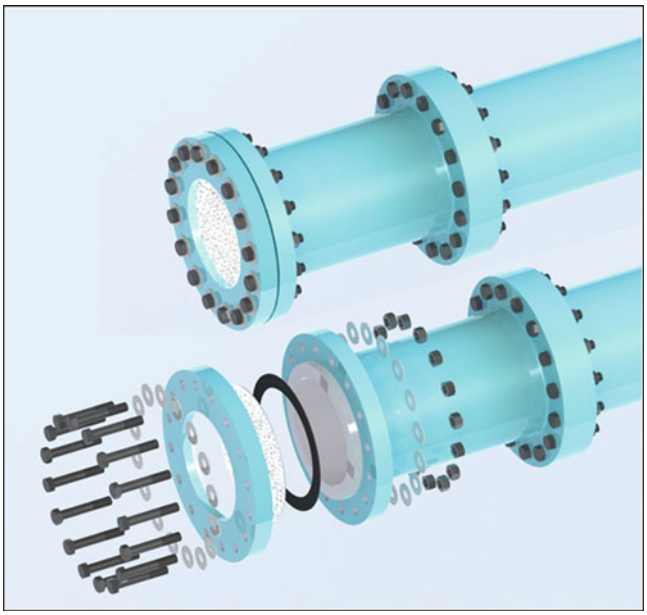

Fig. 13.3 Experimental clamped boundary condition

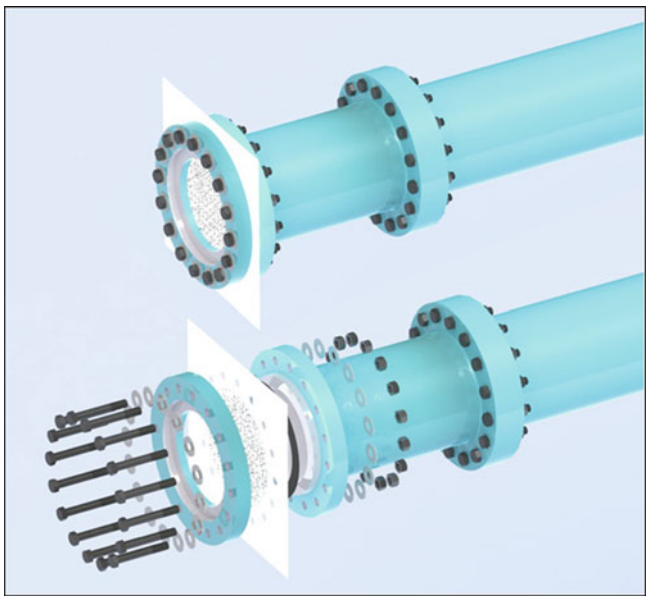

Fig. 13.4 Experimental bolted boundary condition

13.4.2 Bolted

The bolted mounting method was devised to minimize slipping or pulling out of the test specimen from the retaining ring. A larger rectangular test specimen was used and drilled with holes matching the bolt circle in the retaining ring. Figure 13.4 Experimental bolted boundary condition is an illustration of the bolted boundary condition with an exploded view. The gasket and test specimen were placed against the boss on the shock tube working end. The retaining ring was reversed so the rabbet was opposite test specimen. The clamping bolts pass through the test specimen and limit any radial movement. Figure 13.5 Clockwise from top left: composite plate drilled for bolt-through mounting, gasket in place on shock tube working section flange, plate placed on mounting bolts, retaining ring bolted in place shows a plate (in this case composite) drilled and painted for TRC-SDIC, the gasket attached to the plate mounting boss of the shock tube, the plate placed on the bolts, and, finally, the retaining ring bolted in place to complete the setup.

Fig. 13.5 Clockwise from top left: composite plate drilled for bolt-through mounting, gasket in place on shock tube working section flange, plate placed on mounting bolts, retaining ring bolted in place

Fig. 13.6 Detail of quasi-simple support gasket and cable

13.4.3 Quasi-Simply Supported

In this configuration the plate was supported on its back by a rubber gasket reinforced with a wire through its center (see Fig. 13.6). This arrangement can only be considered quasi-simple since in addition to the rubber gasket support, the retaining ring still had to be bolted in place, not tightly though, to hold the test specimen, so the free and unlimited movement in the plane of a true simple support was hindered, but still freer than the clamped mounting. Figure 13.7 is an illustration of the quasi-simply supported mounting with an exploded view. The gasket and the test specimen were placed against the boss on the working end of the shock tube. The quasi-simple support was then placed between the test specimen and the retaining ring. The retaining ring was again flipped so the rabbet faced away from the test specimen and then secured with the bolts. The bolts were made finger-tight to allow more freedom of movement and better mimic a simply supported boundary condition (Fig. 13.7).

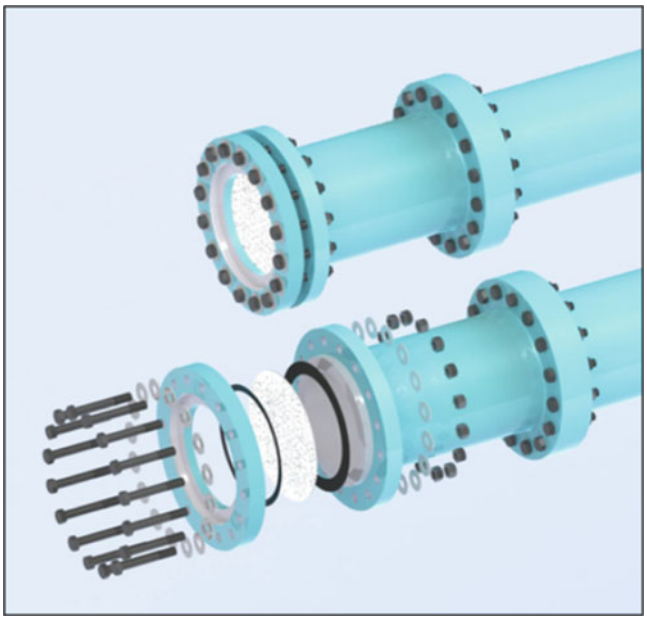

Fig. 13.7 Experimental quasi-simply supported boundary condition

Table 13.1 Parameters and properties of materials tested

Description	Free radius [mm]	Thickness [mm]	Density [kg/m^2]	Elastic modulus [GPa]	Poisson's ratio	Flexural rigidity [Pa m^3]	Bending wave-speed [m/s]	Timescale [ms]
Aluminum	152	3.2	2700	69	0.33	207	4.91	31.05
MIL steel	152	3.2	7900	200	0.30	586	4.83	31.52
Mild steel	152	3.2	7800	200	0.30	586	4.87	31.52
S2-glass/epoxy	152	3.2	1689	22	0.10	58.1	3.29	46.29
S2-glass/epoxy (thin)	152	1.6	1689	22	0.10	7.27	1.65	92.57
S2-glass/ phenolic HJ1	152	3.2	1960	27	0.26	77.2	3.52	43.26

13.5 Test Specimens

The test specimens for the clamped and quasi-simply supported boundary conditions were thin circular plates 380 mm (15″) in diameter. The test specimens for the bolted boundary conditions were thin square plates 610 mm (24″) in width and height. Except where noted, all test specimens were 3.2 mm (1/8″) thick.

The S-2 glass epoxy composite test specimens were manufactured in-house using vacuum assisted resin transfer molding (VARTM). The woven S-2 glass fiber was sealed between two plastic plies along with additional plies of material to assist resin transfer, debagging, etc. In addition to composite materials, military grade steel and mild steel as well as 6060 Aluminum plates were also used as specimens.

Table 13.1 shows the parameters and properties of the materials tested. The S2-glass epoxy plate properties were determined through standard laboratory tests.

In addition to the pressure sensors, high-frequency-response, semiconductor, strain gauges made by Kulite Semiconductor Products (UHP 5000-60); high-frequency-response, semiconductor, backed bar strain gauges made by Micron Instruments (SS-060-033-1000 PB); and general purpose strain gauges made by Micro-Measurements/Vishay Precision Group (CEA-13-125UW-350) were used in various combinations and locations in order to measure the transient strain rate during the impingement of the shock wave. In early tests the strain gauges were surface mounted on the external face of the test specimen (facing outside the tube), but the large accelerations and deformations caused the gauges to detach or otherwise fail well before maximum deformation of the test specimen. Very little usable data was obtained. However, as the fabrication process of the composite plates was advanced, it was possible to embed such sensors into the composite plates during the manufacturing process.

13.6 Optical System and Setup

The experimental technique has been developed based on digital image correlation (DIC). The setup consists of a camera acquiring a split-view (from the left and from the right) of the motion using two separate mirror pairs located at to the left and right of the specimen axis that are inclined and tilted so as to capture the time-dependent motion of the whole plate specimen under blast/shock loading. The optical setup consists of two large size planar primary mirrors A & B viewing the specimen from two opposite locations tilted to about 30° to the specimen as shown schematically in Fig. 13.8. An optical system consisting of a combination of light reflecting (mirrors) and refracting elements (lenses) is called Catadioptric. The setup also includes a single high-frame-rate camera which can accommodate two simultaneous stereo images (the split-view) of the deforming structure on its CMOS chip and therefore it is a real Time-Resolved Catadioptric Stereo Digital Image Correlation (TR-SDIC) system. Figure 13.9 shows a photograph of the TR-SDIC setup. The typical camera setup for TRC-SDIC is shown in Fig. 13.8.

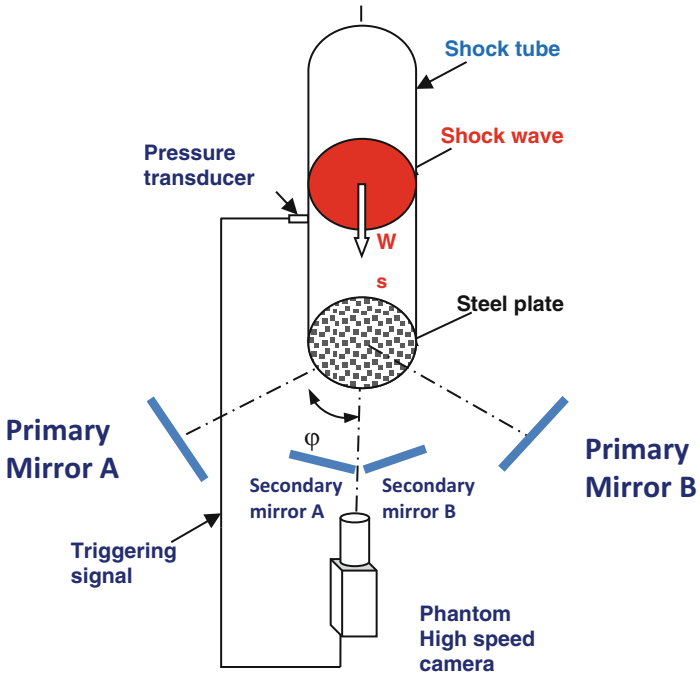

Fig. 13.8 TR-SDIC setup in the shock tube with two pair of mirrors

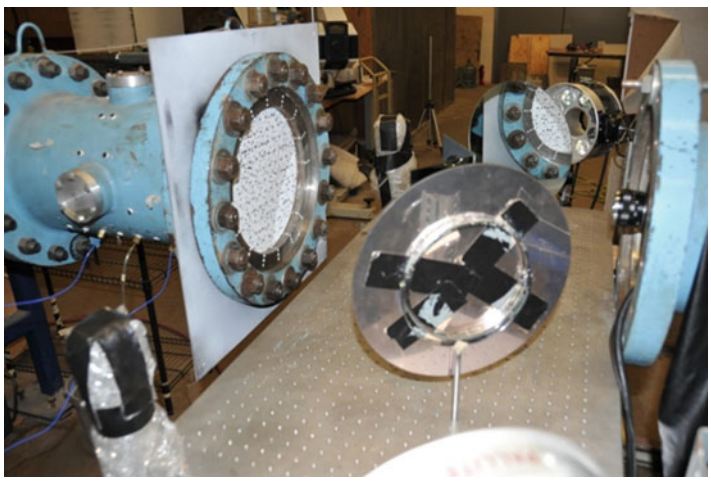

Fig. 13.9 Mirror setup for high-speed video capture of displacement for TRC-SDIC. The lens of the camera can be seen coming out of the tube section at the right

13.7 TRC-SDIC Validation

A major objective of this work is validation of the present optical techniques which will include static as well dynamic measurements of displacements and strain. In the beginning of our work we used a composite plate of 3.2 mm (1/8 in.) thickness with strain-gauges mounted on the external surface of the plate which was also viewed by the camera. However, the strain gauges pop off the plate during the dynamic impact of the shock wave on the internal surface of the plate because of large deformations and high accelerations developing during this dynamic incident. In order to overcome this problem, it was decided to embed the strain gauges in the S-2 glass epoxy 12.7 mm (1/2 in.) thick composite test specimens during in-house using vacuum assisted resin transfer molding (VARTM) fabrication. High-frequency-response, semiconductor, strain gauges made by Kulite Semiconductor Products (UHP 5000-60), high-frequency-response, semiconductor, backed bar strain gauges made by Micron Instruments (SS-060-033-1000 PB), and general purpose strain gauges made by Micro-Measurements/ Vishay Precision Group (CEA-13-125UW-350) were used in various combinations and locations in order to measure the transient strain rate during the impingement of the shock wave. In addition to strain gauges PZT transducers were also embedded which helped measure the frequency response of the test plate. Details of the setup can be found in [25].

Figure 13.10 shows a schematic of the composite plate with the locations of the embedded sensors marked. The strain gauges were mounted in radial/circumferential pairs to measure strain and were positioned carefully below the external surface of the plate under the first fiber layer. The 60 × 60 cm (2 × 2 ft) composite plate was mounted on the end flange of the 304 mm (1 ft) diameter shock tube by using bolts that passed through the specimen as well as the retaining ring to achieve a truer clamped boundary condition for static and dynamic testing.

13.7.1 Static Tests

The shock tube was pressurized slowly and the displacement of the plate was measured by our DIC techniques when the continuously monitored pressure had reached certain levels. The initial static test data from a 3.2 mm (1/8 in.) composite plate were obtained by TRC-SDIC and manually by traversing a digital caliper on a custom-made fixture and measuring at specific points along the specimen diameter. Unlike in the dynamic tests where the mirrors and camera are setup, a calibration shot taken, and the test was run in a short period of time with little chance of the setup moving, the static testing gave many opportunities for the setup to move. To eliminate this potential source of error, calibration shots were taken

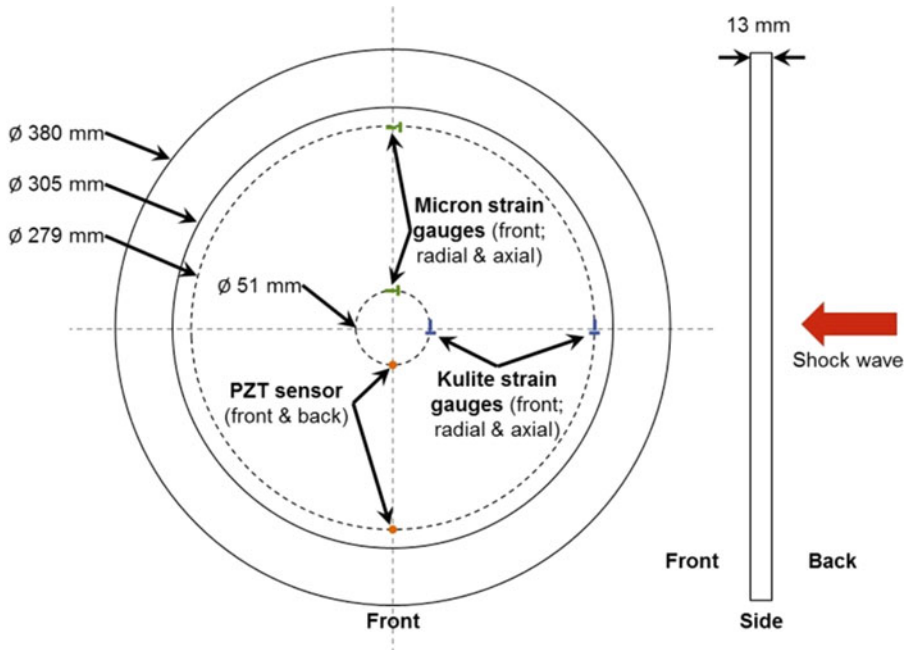

Fig. 13.10 Schematic of S-2 glass epoxy composite plate with locations of embedded sensors (Dimensions in inches)

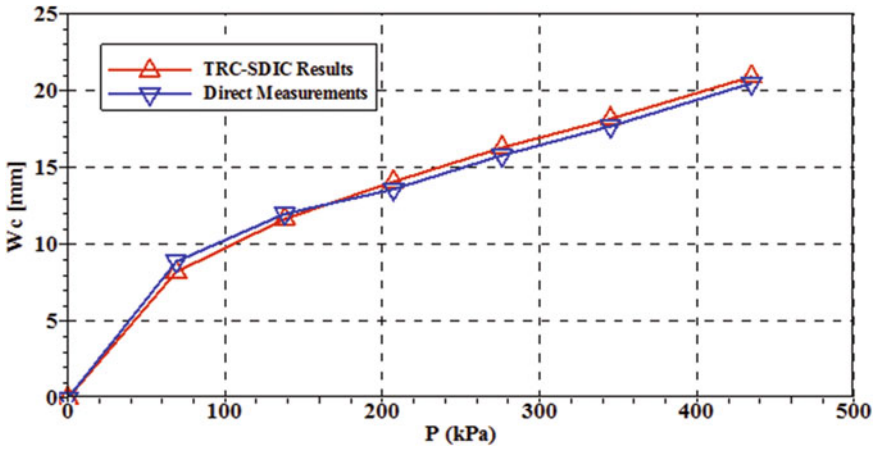

Fig. 13.11 Comparison of axial deformation at the center of the test plate caused by static pressure loading as measured experimentally with results from TRC-SDIC

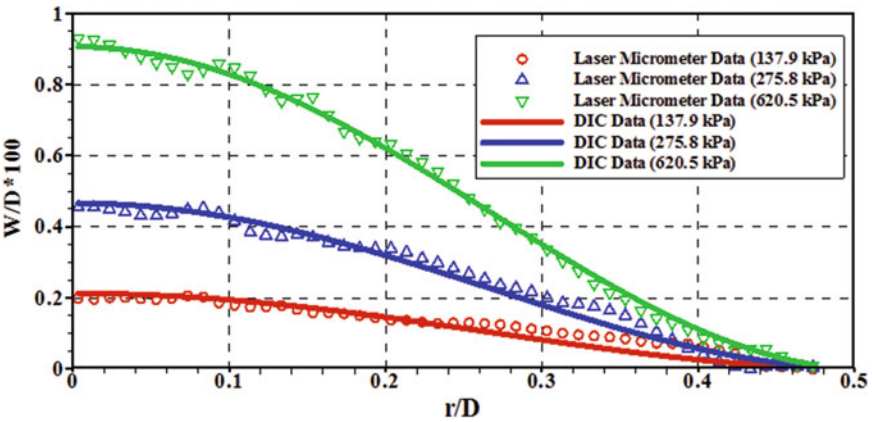

Fig. 13.12 Comparison of out of plane deformation W, during static tests between laser micrometer and DIC data at three different pressure levels. Free diameter of plate: 304 mm (12 in.)

before and after each frame. For these static measurements a laser position micrometer, model OPTO NCDT, was also used to determine the static displacement and deformation of the plate using a triangulation technique.

The results are shown in Fig. 13.11. The deformation at the center of the plate (maximum displacement) is plotted against the static pressure. The agreement between the two approaches is very good, with the largest variance around 8 %. This increases confidence in the TRC-SDIC results.

A second experiment under static conditions was carried out with the 12.7 mm (1/2 in.) composite plate with embedded strain gauges. In this case the displacement of the plate at the specified pressure was measured using the laser micrometer along one diameter. The measurements obtained by TRC-SDIC and the laser micrometer are compared in Fig. 13.12. The results are non-dimensionalized by the diameter of the plate, D. Maximum displacement has been observed at the center of plate at $r/D = 0$ at 620 kPa (90 psi) pressure and was found to be 2.7 mm. The displacement is substantially reduced towards the shock tube wall where the flange is mounted and it is zero at the location of the clamping area. As expected the displacement also depends on the applied static pressure. At the lower pressure levels of 275 kPa and 138 kPa (40 and 20 psi respectively) the measured displacements are also reduced. The laser micrometer data indicate some scatter which is well within the accuracy of the instrument and the uncertainties of measurements. It appears that the DIC data obtained by our optical setup and data processing algorithms based on fitting Bessel functions to the directly measured displacements, agree very well with the data obtained by the laser micrometer.

Comparison of the strains obtained by DIC and the embedded strain-gauges is shown in Fig. 13.13. The radial strain ε_{rr} in cylindrical coordinates is compressive (negative) on the external surface of the plate near the clamping location and changes sign to become tensile (positive) near the center of the plate. The compressive strain near the clamping is, in absolute terms, slightly higher than the tensile strain at the center of the plate. The location where the strain changes sign appears to be at $r/D = 0.283$ at all pressure levels. The strain gauges measured strain at locations below the external surface of the plate and if a linear distribution across the plate thickness, h, is assumed for the strain it will be proportional to $z/h/2$ where z is the location of the strain gauges from the middle plane. Thus $\varepsilon_{rr}(z) = \varepsilon_{rr}(h/2)2z/h$. The half-thickness is $h/2 = 6.4$ mm (1/4 in.). The actual location of the strain gauges, z, is rather difficult to determine accurately first because they can move slightly during the vacuum assisted infusion molding to not only different locations but also to different orientations and second because of their finite

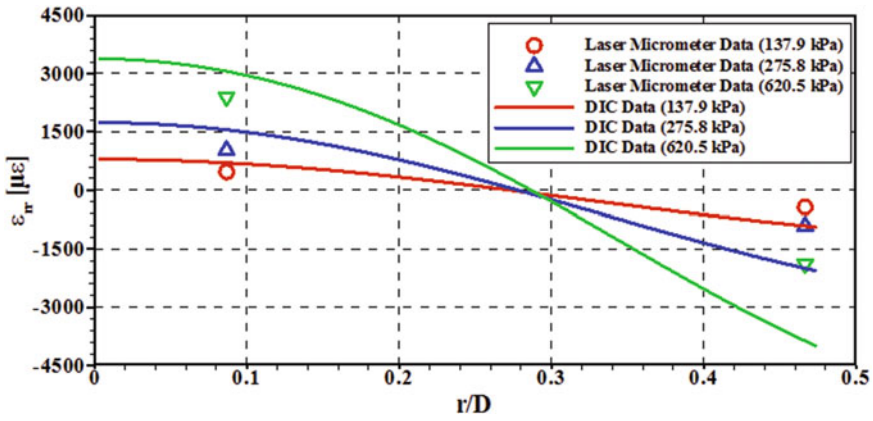

Fig. 13.13 Comparison of in-plane strain ε_{rr} measured by STC-SDIC at the surface and by strain-gauges embedded in the plate, during static at three different pressure levels. Free diameter of plate: 304 mm (12 in.)

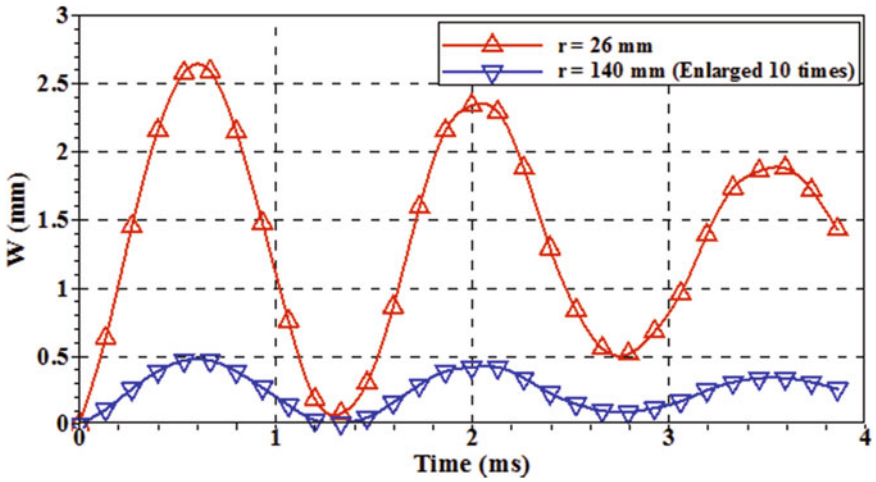

Fig. 13.14 Time-dependent signals of displacement at the locations of the embedded strain gauges obtained by TRC-SDIC during shock impact

thickness. Thus, the strain measurements obtained by the gauges are expected to be lower than the surface strains measured by DIC. This is the case in the data shown in Fig. 13.11b. The gauge located at $r = 0.08D$ consistently measured strains about 20 % less than the surface strains while the gauge at $r = 0.47D$ measured about 40 % of the corresponding surface strains $\varepsilon_{rr}(h/2)$. This relative difference is consistent at all pressures and this consistency provides confidence in the developed TRC-SDIC system.

13.7.2 Dynamic Tests with Shock Impact

A second experiment was carried out in which a shock of 620 kPa (90 psi) strength impinged on the plate and dynamic signals of strain were acquired from the gauges together with time-resolved DIC data. The time-dependent displacement of the plate at the locations of the strain gauges is shown in Fig. 13.14. The plate immediately after the shock impact starts to vibrate in the second mode with a maximum displacement of 2.6 mm at $r = 26$ mm $= 0.084D$ and 0.05 mm at $r = 140$ mm $= 0.46D$. A comparison of the strains measured by the gauges and those obtained by TRC-SDIC is shown in Fig. 13.12b. The two strain signals follow the same periodic variation with time which is due to the plate vibration. This indicates that the TRC-SDIC has the frequency resolution to capture the periodic variation in strain and displacement. At the location $r = 26$ mm the strain sensor measured about 10 % less than DIC's strain and at $r = 140$ mm the strain gauge measured 42 % less strain than DIC. This difference between the dynamic strains is very consistent with the static strains i.e. the strains measured by the embedded gauges are less than the strains at the surface measured by DIC by the same percentage (Fig. 13.15).

The agreement between the displacement data obtained by TRC-SDIC and by the laser micrometer or the caliper in static tests is very good, with the largest variance around 8 %. This increases confidence in the TRC-SDIC results not only in the static case, but also in dynamic cases where, from the TRC-SDIC process perspective there is no difference between static

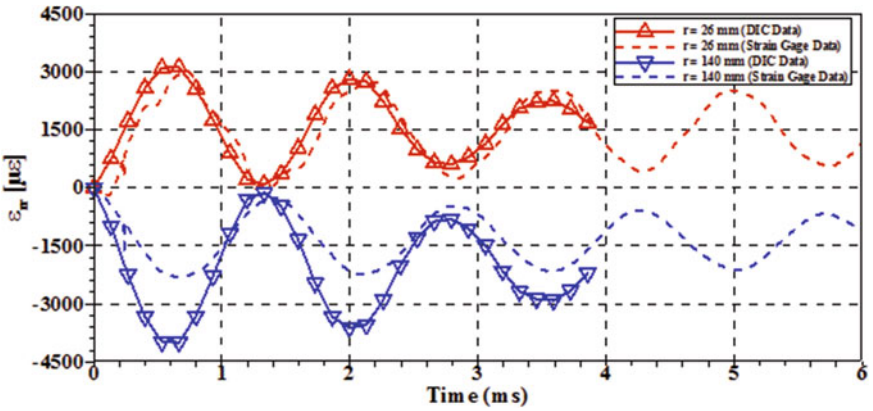

Fig. 13.15 Comparison of time-dependent strain signals obtained from the embedded gauges and from TRC-SDIC during shock impact

and dynamic images since in both cases sequential frames are compared to determine deformations without regard to time. Strain data are more difficult to obtain either by point sensors or global methods and are not very often provided in the literature. In the present work, we demonstrate for the first time a comparison between measurements obtained by embedded strain gauges and by our TRC-SDIC techniques. The agreement between these two methods is very good which provides validation of the approach and establishes confidence in the application of our TRC-SDIC techniques.

13.7.3 Results From the Time-Resolved Catadioptric Stereo Digital Image Correlation—Composite Specimen

The TRC-SDIC technique was used to measure out-of-plane displacement W (z-direction) of the external surface of an in-house manufactured composite specimen. Displacements were calculated from the high-speed camera images that were taken every 0.13 and are shown in Fig. 13.16 Out-of-plane total displacement (z-direction) at 0.13 ms intervals measured by the TRC-SDIC technique (composite specimen). As can be seen, the displacement at the center is increasing after the shock impact and then it decreases. The impact of the shock on the internal surface of the plate sets up a vibration pattern of the plate due to the strong coupling between the flow and the plate [15]. The sequence of the results shown in the frames in Fig. 13.16 Out-of-plane total displacement (z-direction) at 0.13 ms intervals measured by the TRC-SDIC technique (composite specimen) demonstrate an oscillatory behavior of the W-displacement which is mostly positive on the first frames with a maximum amplitude of about 24 mm at the center of plate and close to zero around its periphery nearby the flange. By the eighth frame the amplitude is reduced to 20–22 mm and another vibration cycle begins.

13.8 The Effects of Boundary Conditions

Despite what would appear to be a firmly clamped boundary condition, evidence of the test specimen slipping or pulling out slightly from the retaining ring was observed. For dynamic tests a pattern of radial scratches was often observed on the clamped part of the test specimen. These scratches became more prominent at higher pressures. Additionally some of the dynamic tests appeared to be more non-linear than expected. The results showed that the torque on the bolts applying the pressure to the retaining ring had a significant impact on the displacement of the test specimen. Using a steel plate allowed maximum torque (given the available torque wrench) to be applied without concern for crushing or initiating damage in the test specimen.

Since it was now clear that the regular boundary condition was not acting as a clamped condition additional methods for mounting the test specimens were developed as described above and additional tests were performed to see the effects of those conditions and to better classify the original clamped condition. Figure 13.17 shows the maximum center displacement for aluminum, steel, and composite plates under clamped, bolted, and quasi-simple boundary conditions. Exact repetition of the pressure level is difficult to achieve so some interpretation is required; however, the trends are as expected based on the relative holding power of the retaining ring normal to the shock tube axis. Figure 13.18 shows the elongation of the plate across the diameter. This elongation (or membrane stretching) data helps measure the slipping and contributes to calculating more accurate strain calculations.

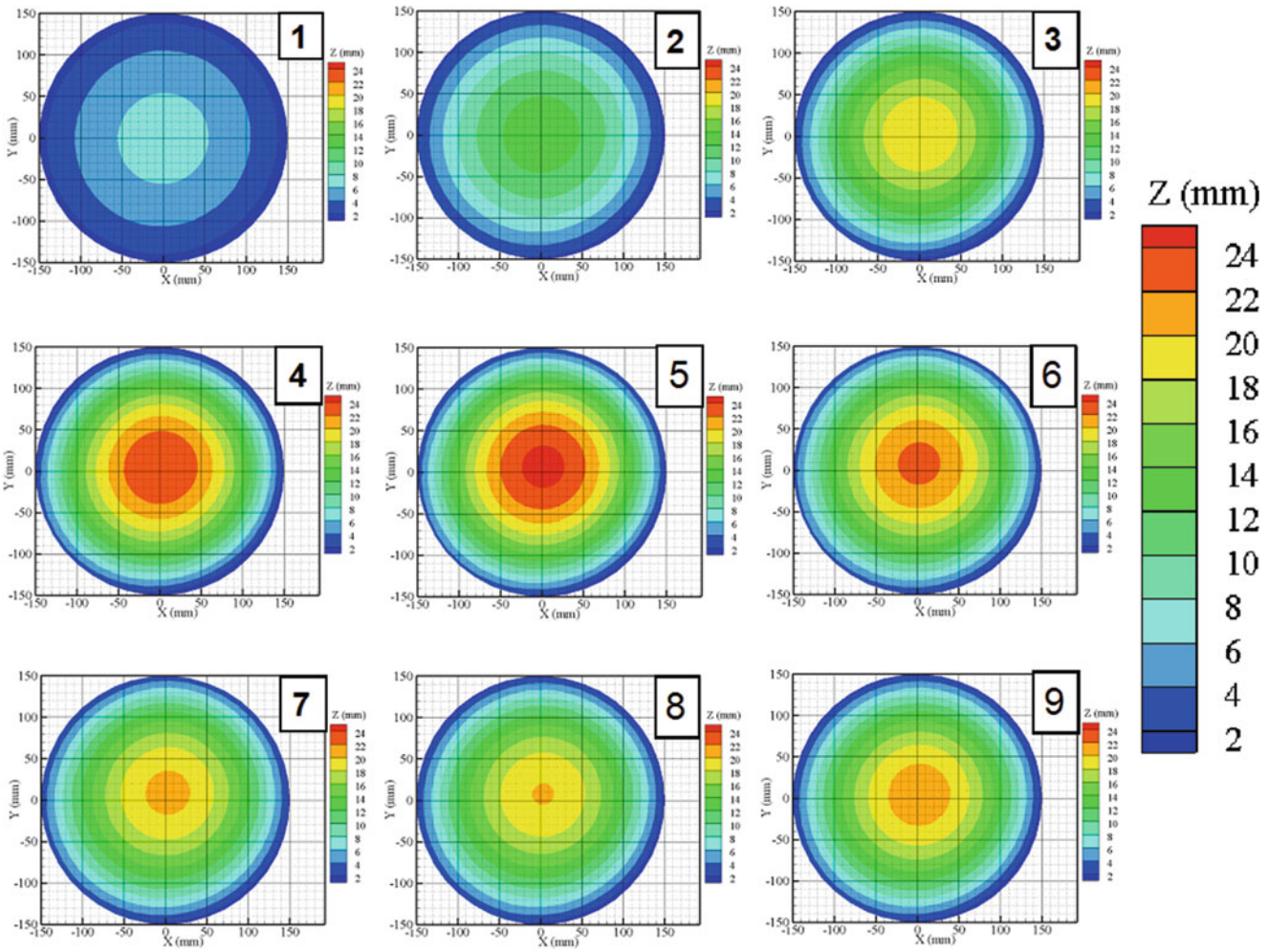

Fig. 13.16 Out-of-plane total displacement (z-direction) at 0.13 ms intervals measured by the TRC-SDIC technique (composite specimen)

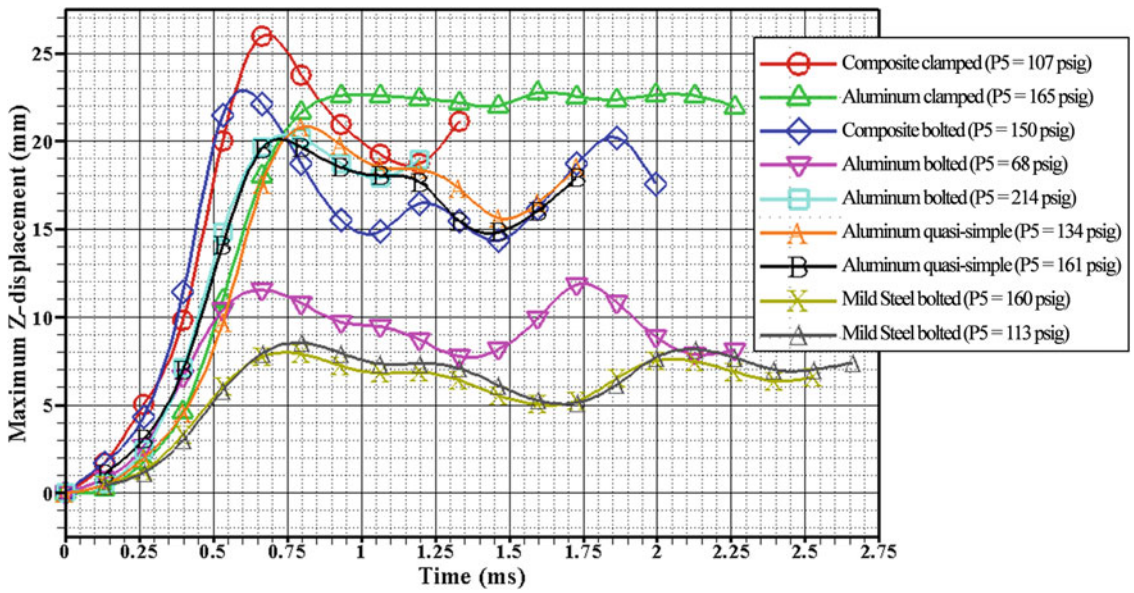

Fig. 13.17 Maximum center displacement as measured by DIC

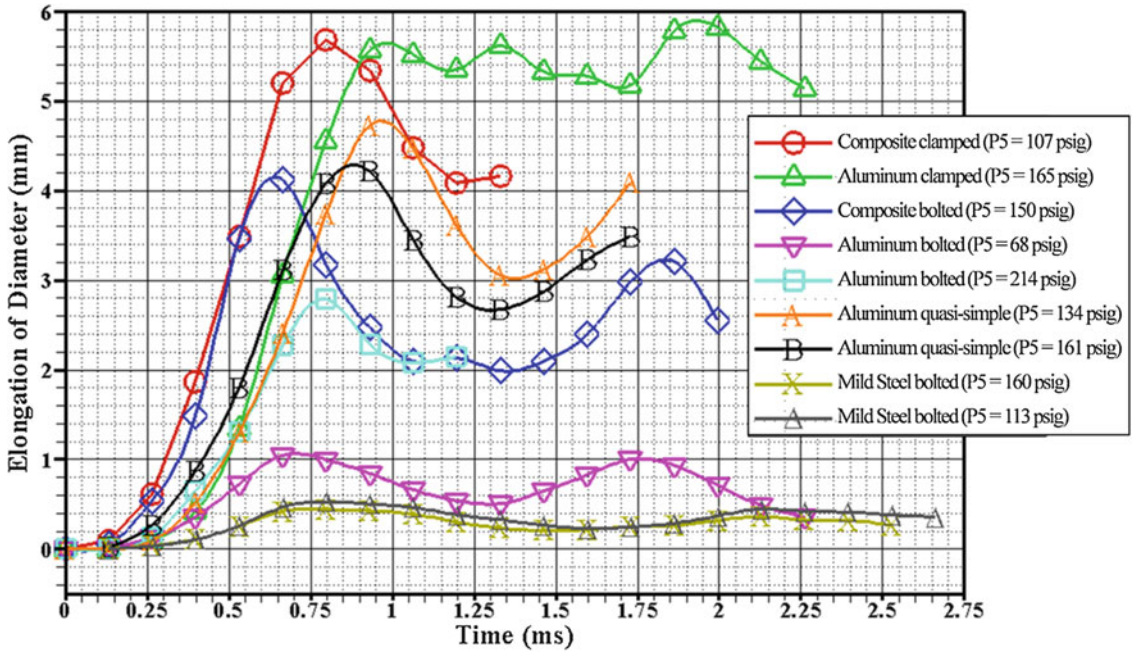

Fig 13.18 Elongation across the diameter as measured by DIC

13.9 Conclusions

In the present research we tested experimentally S2 HJ1 phenolic and S2 glass epoxy composites and provided details of their interaction with shock-waves For comparison of monolithic material response to similar loadings, tests were also conducted with aluminum specimens. A Time-Resolved Catadioptric Stereo Digital Image Correlation (TRC-SDIC) process was developed from traditional DIC techniques to determine the three-dimensional deformation of the specimens using a single camera. The TRC-SDIC process provided time-dependent full-field deformation measurements and allowed calculation of full-field strains. The system is capable of providing time dependent information of three component displacement vectors on two dimensional surfaces undergoing rapid deformation. The present layout offers several advantages over traditional systems with two different cameras:

1. It provides identical system parameters for the two views which minimizes their differences and thus facilitating robust stereo matching.
2. It reduces calibration time since only one camera is used.
3. Its cost is substantially lower than the cost of a system with two cameras.

In addition, in the present work we developed a calibration method to account for the motion of the mirrors during the experiments caused by acoustic waves emitted by the vibrating specimens and we experimented with the use of shape modes to filter/smooth/fit the experimental data with Bessel functions for elastic deformations.

At the end, we carried out extensive validation tests of our optical techniques which included comparisons with static and dynamic data obtained from embedded sensors in the specimens at the same time the images were acquired.

The effect boundary conditions i.e. the type of mounting the specimen to the end wall flange of the shock tube was investigated. Interactions with clamped, bolted or quasi-simply supported plates subjected to dynamic loading have been configured. Bolted specimens demonstrated the least maximum dynamic displacement and shortest elongation along one diameter

This material is based upon work supported by the US Department of Defense under Contract No. W56HZV-09-C-0569

References

1. Sutton, M., Wolters, W., Peters, W., et al.: Determination of displacements using an improved digital correlation method. Image Vis. Comput. **1**, 133–139 (1983). doi:10.1016/0262-8856(83)90064-1
2. Kahn-Jetter, Z.L., Chu, T.C.: Three-dimensional displacement measurements using digital image correlation and photogrammic analysis. Exp. Mech. **30**, 10–16 (1990)
3. Sutton, M.A., Orteu, J.-J., Schreier, H.W.: Image correlation for shape, motion and deformation measurements: basic concepts, theory and applications. Springer, New York (2009)
4. Goshtasby, A., Gruver, W.A.: Design of a single-lens stereo camera system. Pattern Recogn. **26**, 923–937 (1993)
5. Inaba, M., Hara, T., Inoue, H.: A stereo viewer based on a single camera with view-control mechanisms. In: Intell Robots Systems 93 IROS 93 Proceedings of the 1993 IEEE/RSJ International Conference on, vol. 3, pp. 1857–1865. doi:10.1109/IROS.1993.583888
6. Gluckman, J., Nayar, SK.: Planar catadioptric stereo: Geometry and calibration. In: Computer Vision and Pattern Recognition, 1999. IEEE Computer Society Conference on, vol. 1, (1999)
7. Gluckman, J., Nayar, S.: Catadioptric stereo using planar mirrors. Int. J. Comput. Vis. **44**, 65–79 (2001). doi:10.1023/A:1011172403203
8. Gluckman, J., Nayar, S.K.: Rectified catadioptric stereo sensors. IEEE Trans. Pattern Anal. Mach. Intell. **24**, 224–236 (2002)
9. Kreizer, M., Liberzon, A.: Three-dimensional particle tracking method using FPGA-based real-time image processing and four-view image splitter. Exp. Fluids **50**, 613–620 (2011). doi:10.1007/s00348-010-0964-3
10. Pankow, M., Justusson, B., Waas, A.M.: Three-dimensional digital image correlation technique using single high-speed camera for measuring large out-of-plane displacements at high framing rates. Appl. Opt. **49**, 3418–3427 (2010)
11. Elzawawy, A.: Time resolved particle image velocimetry techniques with continuous wave laser and their application to transient flows. Ph.D. Thesis, City University of New York (2012)
12. Briassulis, G., Agui, J.H., Andreopoulos, J., Watkins, C.B.: A shock tube research facility for high-resolution measurements of compressible turbulence. Exp. Thermal. Fluid Sci. **13**, 430–446 (1996). doi:10.1016/S0894-1777(96)00097-0
13. Subramaniam, K.V., Nian, W., Andreopoulos, Y.: Blast response simulation of an elastic structure: Evaluation of the fluid–structure interaction effect. Int. J. Impact Eng. **36**, 965–974 (2009). doi:10.1016/j.ijimpeng.2009.01.001
14. Pankow, M., Justusson, B., Salvi, A., Waas, A., Yen, C.-F., Ghiorse, S.: Shock response of 3d woven composites: an experimental investigation. Compos Struct **93**(5), 1337–1346 (2011). doi:10.1016/j.compstruct.2010.10.021
15. Gong, M., Andreopoulos, Y.: Coupled fluid-structure solver: The case of shock wave impact on monolithic and composite material plates. J. Comput. Phys. **228**, 4400–4434 (2009). doi:10.1016/j.jcp.2009.03.009
16. Kazemi-Kamyab, V., Subramaniam, K., Andreopoulos, Y.: Stress transmission in porous materials impacted by shock waves. J. Appl. Phys. **109**, 013523 (2011). doi:10.1063/1.3517791
17. Xia, S., Gdoutou, A., Ravichandran, G.: Diffraction assisted image correlation: A novel method for measuring three-dimensional deformation using Two-dimensional digital image correlation. Exp. Mech. **53**, 755–765 (2013). doi:10.1007/s11340-012-9687-0
18. Jahnke, D., Andreopoulos, Y.: Development of a time-resolved catadioptric stereo digital image correlation technique for the study of blast loading of composite material structures. ASME Conf. Proc. **2011**, 153–162 (2011)
19. Tiwari, V., Sutton, M.A., McNeill, S.R., et al.: Application of 3D image correlation for full-field transient plate deformation measurements during blast loading. International Journal of Impact Engineering 3**6**, 862–874 (2009). doi: 10.1016/j.ijimpeng.2008.09.010
20. Tsai, R.: An efficient and accurate camera calibration technique for 3D machine vision. In: Proceeding of the IEEE Conference on Computer Vision and Pattern Recognition, Miami Beach, FL, pp. 364–374, (1986)
21. Justusson, B., Pankow, M., Heinrich, C., Rudolph, M., Waas, A.M.: Use of a shock tube to determine the bi-axial yield of an aluminum alloy under high rates. Int. J. Impact Eng. **58**, 55–65 (2013)
22. Lowe, D.G.: Object recognition from local scale-invariant features. In: Computer Vision 1999 Proceedings of the Seventh IEEE International Conference on, vol. 2, pp. 1150–1157 (1999)
23. Wieneke, B.: Stereo-PIV using self-calibration on particle images. Exp. Fluids **39**, 267–280 (2005)
24. Jahnke, D., Azadeh-Ranjbar, V., Andreopoulos, Y.: Composite plates' response to shock wave impact. Compos. B, Submitted (2015)
25. Jahnke, D.: The effect of shockwave impingement on thin, woven glass fiber reinforced, polymer composite plates. Ph.D. Thesis, The City College of New York—Grove School of Engineering (2014)
26. Wang, E., Shukla, A.: Analytical and experimental evaluation of energies during shock wave loading. Int. J. Impact Eng. **37**(12), 1188–1196 (2010). doi:10.1016/j.ijimpeng.2010.07.003
27. Gong, M. Mutual interactions between shock waves and structures. PhD Thesis, City University of New York (2006)
28. Pankow, M., Justusson, B., Waas, A.M.: Three-dimensional digital image correlation technique using single high-speed camera for measuring large out of-plane displacements at high framing rates. Appl. Optics **17**, 3418–3427 (2010)
29. Gibson, R. F., Chen, Y., and Zhao, H.: Improvement of Vibration Damping Capacity and Fracture Toughness in Composite Laminates by the Use of Polymeric Interleaves, J. Eng. Mater. Technol., **123**(3), pp. 309–314 (2001)
30. Koratkar, N. A., Suhr, J., Joshi, A., Kane, R. S., Schadler, L. S., Ajayan, P. M., and Bartolucci, S.: Characterizing energy dissipation in single-walled carbon nanotube polycarbonate composites, Appl. Phys. Lett., **87**(6), p. (2005)
31. Zhou, X., Shin, E., Wang, K. W., and Bakis, C. E.: Interfacial damping characteristics of carbon nanotube-based composites, Dev. Carbon Nanotube Nanofibre Reinf. Polym., **64**(15), pp. 2425–2437 (2004)
32. Rajoria, H., and Jalili, N.: Passive vibration damping enhancement using carbon nanotube-epoxy reinforced composites, Compos. Sci. Technol., **65**(14), pp. 2079–2093 (2005)
33. Briassulis, G., Agui, J. H., Andreopoulos, J., and Watkins, C. B.: A shock tube research facility for highresolution measurements of compressible turbulence, Exp. Therm. Fluid Sci., **13**(4), pp. 430–446 (1996)
34. Andreopoulos, Y., Agui, J. H., and Briassulis, G.: Shock Wave Turbulence Interactions, Annu Rev Fluid Mech, **32**(1), pp. 309–345 (2000)
35. Briassulis, G., Agui, J. H., and Andreopoulos, Y.: The structure of weakly compressible grid-generated turbulence, J. Fluid Mech., 432, pp. 219–283 (2001)